PHYSICAL REVIEW FLUIDS **5**, 053102 (2020)

Bundled slender-body theory for elongated geometries in swimming bacteria

Bin Liu[*] and Jeremias Gonzalez
Department of Physics, University of California, Merced, Merced, California 95343, USA

(Received 11 June 2018; accepted 30 April 2020; published 22 May 2020)

Size and shape of a living microorganism have been recognized as important factors for its movement through a viscous fluid. Understanding how subtle variations in cellular geometry affect the hydrodynamic forces requires solving three-dimensional (3D) Stokes equations, e.g., by resolving an object's 2D surface in a boundary integral method. A reduction of these computational costs involves using available symmetries to simplify the boundary geometries, such as representing a slender body by its body centerline, known as the slender-body theory. Here, we extend the range of the aspect ratio that can be treated by a standard slender-body theory, by representing the body with a bundle of thin filaments that each still approximately satisfies the slender-body criteria. We show that this bundled slender-body theory can be used to determine the dependency of hydrodynamic forces on varying geometric factors of a moving object. As a direct application of this method, we study the optimized kinematics of a monotrichous bacterium that has a curved cell body and swims by rotating a helical flagellum. We show that the curvature in its cell body can play a nontrivial role in the swimming motility, depending on the chirality emerging from the cell-flagellum alignment.

DOI: 10.1103/PhysRevFluids.5.053102

I. INTRODUCTION

Microorganisms explore aqueous environments through engagements of filamentlike motile organelles, including the prokaryotic flagella, and the eukaryotic motile cilia [1,2]. Due to the negligible inertia of fluids at such a small scale, these motile organelles operate by introducing nonreciprocal locomotions to overcome the kinematic reversibility [1]. As a well-known example, the bacterium *Escherichia coli* acquires motility by rotating a bundle of helical flagella that propels the surrounding fluid like a corkscrew [3]. In addition to the variety of motile organelles, microorganisms also appear in various shapes [4]. Among all possible morphologies, curved and helical bodies have been of particular interest regarding their potential significance for swimming motilities [5–9]. Understanding the full roles of geometries in such microswimming ultimately relies on solving a three-dimensional (3D) Stokes equation, subjected to the no-slip boundary condition on both the cell wall and its motile organelles.

A full 3D Stokes simulation of the microswimmer is regarded computationally expensive due to the high spatial degree of freedom (DOF) for an arbitrary 3D object, associated with the required 2D surface grids for decent numerical convergence [10–14]. In practice, symmetry-based strategies have been employed to reduce such a high DOF and thus the computational cost. For instance, an approximate cylindrical symmetry in the near field of a slender body has been utilized to reduce its degree of freedom from a surface mesh to a linear mesh along the body centerline [15–17]. These are known as the slender-body theories (SBT) that are widely applied to capture the hydrodynamic interactions along the thin motile organelles [18–20]. Meanwhile, a helical symmetry

---

[*] bliu27@ucmerced.edu

has been applied for reducing the spatial DOF from a helical filament to its cross section [21,22]. Despite these successes, such reduction strategies cannot be directly executed on a freely swimming microorganism, where such symmetries are no longer satisfied due to the hydrodynamic interactions between the motile organelles and the cell body. As a workaround of such lacking symmetries, it has been shown that an irregular object can be usefully decomposed into a number of small particles, e.g., spheres [23,24]. In these approaches, the hydrodynamic interactions among these composite objects satisfy higher-order symmetries, achieved through multipole moment expansions. Additionally, a hybrid method that bridges a full 3D modeling of the cell body and a slender-body treatment of the motile organelles has been introduced to the studies of swimming microorganisms [25]. While versatile, these approaches all require expert care for allocating the composite particles or the mesh nodes for decent computing accuracies. Meanwhile, the characteristic geometry of an object, e.g., an elongated cell body [26], can hardly be implemented in these approaches, leading to their relatively higher computational costs in studying the geometric effects in microswimmers.

Here, we investigate a reduction approach that decomposes an object into a number of subunits while still incorporating its elongated geometry. Such a reduction is achieved by representing an elongated object by a bundle of slender bodies to be solved by the SBT. When separated far enough, this bundled slender-body theory (bSBT) provides a decent estimation of the hydrodynamic forces on the modeled object, suggesting that the cylindrical symmetry in the SBT is still justified for each subunit. This bSBT thus works seamlessly for a system that includes both an elongated body and a thin filament, such as a swimming microorganism, where every object can be represented by slender bodies. To demonstrate such a capacity, we apply bSBT to swimming bacteria in both straight and curved cell shapes. This paper is organized as follows. We first review the SBT and examine its capacity for a finite filament. We then construct the bSBT from the regular SBT and investigate its parameter space for its optimal performance and validation purposes. Finally, we apply the bSBT to a study of swimming bacteria and show the nontrivial roles of cell curvatures in bacterial motilities.

II. SLENDER-BODY THEORY FOR FINITE SLENDER BODIES

To view the roles of symmetry in reducing the DOF for computation, we adopt the SBT introduced by Keller and Rubinow [16], which is deduced upon a cylindrical symmetry satisfied by an infinitely thin body.

In this version of the SBT, a finite filament of length L, immersed in a fluid with viscosity μ, has a circular cross section with radius $a(s)$ at a displacement s along the body centerline from a tip of the body (Fig. 1). A coordinate $\mathbf{x}(s, \rho, \theta)$ is defined by traveling a displacement s along the centerline and moving outward with polar coordinates ρ and θ. The position of the body centerline is given by $\mathbf{x}_0(s) = \mathbf{x}(s, 0, \theta)$. Considering the filament thin, the flow field near its surface should approach the solution of an infinite cylinder aligned along the tangential direction of the filament, which is free to translate (at velocity $\mathbf{v}$), rotate (at angular velocity $\boldsymbol{\omega}$), and dilate (at expansion rate $\dot{a}$). This near-field flow velocity $\mathbf{u}(\mathbf{x})$ can thus be approximated as an asymptotic expansion from the center of the cross section in polar coordinates, also known as the inner expansion [16]:

$$\begin{aligned}\mathbf{u}(\mathbf{x}) \sim\ & \mathbf{v}(s) + \hat{\mathbf{i}}g(s)\ln\frac{\rho}{a(s)} + \hat{\mathbf{j}}h(s)\left[\ln\frac{\rho}{a(s)} + \frac{1}{2}\left(1 - \frac{a^2(s)}{\rho^2}\right)\right]\\ & - (\hat{\mathbf{j}}\cos^2\theta + \hat{\mathbf{k}}\sin\theta\cos\theta)h(s)\left(1 - \frac{a^2(s)}{\rho^2}\right)\\ & + (-\hat{\mathbf{j}}\sin\theta + \hat{\mathbf{k}}\cos\theta)\frac{\omega(s)a^2(s)}{\rho} + (\hat{\mathbf{j}}\cos\theta + \hat{\mathbf{k}}\sin\theta)\frac{a(s)\dot{a}(s)}{\rho},\end{aligned} \tag{1}$$

where coordinates $(\hat{\mathbf{i}}, \hat{\mathbf{j}}, \hat{\mathbf{k}})$ are defined by the longitudinal direction $(\hat{\mathbf{i}})$ and the translational direction (prescribed in the "$\hat{\mathbf{i}}$-$\hat{\mathbf{j}}$" plane) of the filament. Here the unknown functions g and h are determined by matching the singular terms (for vanishing ρ) in the above inner expansion to that in a far-field

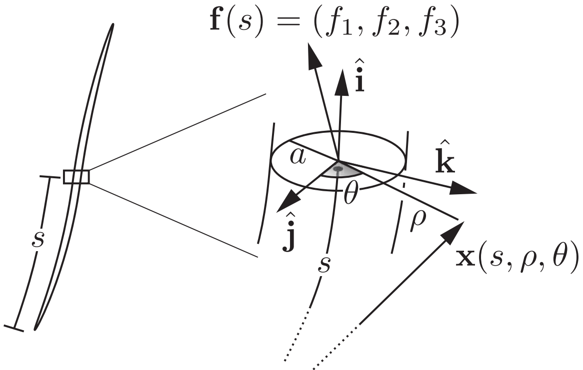

FIG. 1. Schematic presentation of the slender-body theory (SBT). The zoomed-in view shows a circular cross section of a slender body with a radius a, displaced by an arc length s along its body centerline. Unit vectors $(\hat{\mathbf{i}}, \hat{\mathbf{j}}, \hat{\mathbf{k}})$ define a local coordinate system, with the tangential direction of the body centerline along $\hat{\mathbf{i}}$ and the translational direction lying in the "$\hat{\mathbf{i}}$-$\hat{\mathbf{j}}$" plane. In the SBT, a linear integral of the singular force $\mathbf{f}(s)$, known as the stokeslet, along the entire body centerline contributes to the flow velocity located at $\mathbf{x}$ through a Green's function.

approximation of the same flow field [27], also known as the outer expansion [16]:

$$\mathbf{u}(\mathbf{x}) \sim \mathbf{u}_0(\mathbf{x}) + \frac{1}{8\pi\mu}\int_0^L \left[\frac{\mathbf{f}(s')}{|\mathbf{R}|} + \frac{\mathbf{R}\mathbf{R}\cdot\mathbf{f}(s')}{|\mathbf{R}|^3} + \frac{\boldsymbol{\gamma}(s')\times\mathbf{R}}{|\mathbf{R}|^3}\right]ds', \tag{2}$$

where $\mathbf{u}_0$ is the ambient fluid velocity and $\mathbf{R} = \mathbf{x} - \mathbf{x}_0(s')$ is the displacement of position $\mathbf{x}$ from the body centerline. The integrand in the above equation is singular, composed of a stokeslet ($\mathbf{f}$) and a rotlet ($\boldsymbol{\gamma}$), corresponding to a singular point source due to a force and a torque, respectively. Considering a prolate spheroid with radius $a(s) = \frac{2a\sqrt{s(L-s)}}{L}$, the singularity in the above integral is replaced by an asymptotic function of the normalized filament thickness $\epsilon = a/L$. The translational movement of the filament $\mathbf{v}(s)$ relative to the ambient flow $\mathbf{u}_0(s)$ can thus be expressed as

$$\mathbf{v}(s) - \mathbf{u}_0(s) = \frac{1}{8\pi\mu}[\mathbf{A}[\mathbf{f}](s) + \mathbf{B}[\boldsymbol{\gamma}](s)], \tag{3}$$

with two terms $\mathbf{A}[\mathbf{f}](s)$ and $\mathbf{B}[\boldsymbol{\gamma}](s)$ denoting the contributions of the stokeslet and the rotlet, respectively [16]:

$$\begin{aligned}\mathbf{A}[\mathbf{f}](s) = {} & \{-(2\ln\epsilon + 1)[\mathcal{I} + \hat{\mathbf{i}}(s)\hat{\mathbf{i}}(s)] + 2[\mathcal{I} - \hat{\mathbf{i}}(s)\hat{\mathbf{i}}(s)]\}\cdot\mathbf{f} \\ & + \int_0^L \left\{\frac{\mathbf{f}(s')}{|\mathbf{R}_0|} - \frac{[\mathcal{I} + \hat{\mathbf{i}}(s)\hat{\mathbf{i}}(s)]\cdot\mathbf{f}(s)}{|s - s'|}\right\}ds' + \int_0^L \frac{\mathbf{R}_0\mathbf{R}_0\cdot\mathbf{f}(s')}{|\mathbf{R}_0|^3}ds'\end{aligned} \tag{4}$$

and

$$\mathbf{B}[\boldsymbol{\gamma}](s) = \int_0^L \left[\frac{\boldsymbol{\gamma}(s')\times\mathbf{R}_0}{|\mathbf{R}_0|^3} - \frac{1}{2}\frac{\boldsymbol{\gamma}(s)\times\hat{\mathbf{i}}_s(s)}{|s - s'|}\right]ds'. \tag{5}$$

Here, $\mathbf{R}_0 = \mathbf{x}_0(s) - \mathbf{x}_0(s')$ is the separation vector between two points on the body centerline and $\mathcal{I}$ is the identity matrix. It is worth noting that the above two contributions (from stokeslets and rotlets) are unmatched in the order of their accuracies with respect to the filament radius. $\mathbf{A}[\mathbf{f}](s)$, dependent on the stokeslet, is of the order $O(a)$, while $\mathbf{B}[\boldsymbol{\gamma}](s)$, dependent on the rotlet, is of the order $O(a^2)$ [17]. To fully expand contributions to the same extent, in addition to the rotlet term there would also need to be terms from the source, stresslet, and quadrupole contributions [17].

Considering a thin filament, the rotlet $\boldsymbol{\gamma}$ along the filament can also be simplified as $\boldsymbol{\gamma}(s) = (8\pi\mu)\frac{1}{2}a^2(s)\boldsymbol{\omega}(s)$, where $\boldsymbol{\omega}(s) = \boldsymbol{\omega}\cdot\hat{\mathbf{i}}(s)\hat{\mathbf{i}}(s)$ is the projected angular velocity along the body centerline. Given the movement of the filament relative to the ambient flow $\mathbf{v}(s) - \mathbf{u}_0(s)$ and its angular velocity $\boldsymbol{\omega}$, the stokeslets $\mathbf{f}(s)$ (or the force per unit length) on the filament are readily computed by discretizing Eq. (3). The resulting net force $\mathbf{F}$ and net torque $\boldsymbol{\Gamma}$ on the filament can thus be obtained as

$$\mathbf{F} = -\int_0^L \mathbf{f}(s)ds \tag{6}$$

and

$$\boldsymbol{\Gamma} = -\int_0^L [\mathbf{x}_0(s)\times\mathbf{f}(s) + \boldsymbol{\gamma}(s)]ds. \tag{7}$$

To demonstrate how well the above cylindrical symmetries (assumed in the SBT) are satisfied for a finite filament, we consider a prolate spheroid with a half-period helical body centerline at a pitch angle θ_0 (here, $\theta_0 = \pi/4$), i.e., $\mathbf{x}_0(s) = [x(s), y(s), z(s)] = L\,\sin\theta_0[\frac{1}{\pi}\sin(\frac{\pi s}{L}), -\frac{1}{\pi}\cos(\frac{\pi s}{L}), (\frac{s}{L}-\frac{1}{2})\cot\theta_0]^\top$. The spheroid is allowed to translate at a velocity $\mathbf{V}$ and rotates at an angular velocity $\boldsymbol{\omega}$. The corresponding velocity and rotlet along the body centerline are thus prescribed as $\mathbf{v}(s) = \boldsymbol{\omega}\times\mathbf{x}_0(s) + \mathbf{V}$ and $\boldsymbol{\gamma}(s) = (8\pi\mu)[\boldsymbol{\omega}\cdot\hat{\mathbf{i}}(s)\hat{\mathbf{i}}(s)]a^2(s)/2$, respectively. Figure 2 shows the hydrodynamic forces computed by the SBT (in solid lines), which are compared to the results from a 3D simulation using a boundary element method (BEM) without any symmetry-based reductions (in dashed lines) [22]. Here, the slenderness of the filament is characterized by the ratio between the semiminor and the semimajor axes as $a/b = 2/\epsilon$. For $a/b = 0.1$, the SBT results agree reasonably well with the BEM solution, demonstrating the validity of the cylindrical symmetry [Eq. (1)] and the dominating far-field hydrodynamic interactions [Eq. (2)] in the SBT. For $a/b = 0.2$, the result of the SBT deviates significantly from the BEM solution, consistent with the poorly satisfied SBT assumptions for a finite filament.

III. BUNDLED-SLENDER-BODY APPROACH

To extend the SBT to an elongated object with a finite aspect ratio, we replace the object with a number of slender bodies, following its body centerline. Figure 3 shows a schematic of this replacement. A body (with semiminor axis a) is replaced by a bunch of slender spheroids (in red) as subunits, which are enclosed by the same exterior envelope (in blue). The semiminor axis of each spheroid is given by $a_s = \phi a\,\sin(\pi/N_s)/[\phi + \sin(\pi/N_s)]$, where N_s (here $N_s = 3$) is the number of these spheroids and ϕ is a fraction factor such that $\phi = 1$ for close packing of filaments and $a_s \approx \phi a$ for $\phi \ll 1$. The body centerlines of these filaments are thus formulated by

$$\mathbf{x}_s(s,\varphi_i) = \mathbf{x}_0(s) + \hat{r}(s,\varphi_i)a(s)(1 - a_s/a) \tag{8}$$

and

$$\hat{r}(s,\varphi_i) = \mathcal{R}(s)\cdot\begin{pmatrix}\cos\varphi_i\\ \sin\varphi_i\\ 0\end{pmatrix}, \quad i = 1, 2, \ldots, N_s, \tag{9}$$

where $\mathcal{R}(s)$ is a rotation operation determined by the Frenet-Serret frame along the body centerline and $\varphi_i = \frac{2(i-1)\pi}{N_s}$. Considering these filaments are sufficiently far (to be justified later), the outer expansion from the SBT can still be applied to each filament by approximating the hydrodynamic contribution from other filaments with a modified ambient flow. The outer expansion on the αth slender body thus becomes

$$\mathbf{u}(\mathbf{x}) \sim \mathbf{u}_\alpha(\mathbf{x}) + \frac{1}{8\pi\mu}\int_0^{L_\alpha}\left[\frac{\mathbf{f}(s_\alpha)}{|\mathbf{R}_\alpha|} + \frac{\mathbf{R}_\alpha\mathbf{R}_\alpha\cdot\mathbf{f}(s_\alpha)}{|\mathbf{R}_\alpha|^3} + \frac{\boldsymbol{\gamma}(s_\alpha)\times\mathbf{R}_\alpha}{|\mathbf{R}_\alpha|^3}\right]ds_\alpha. \tag{10}$$

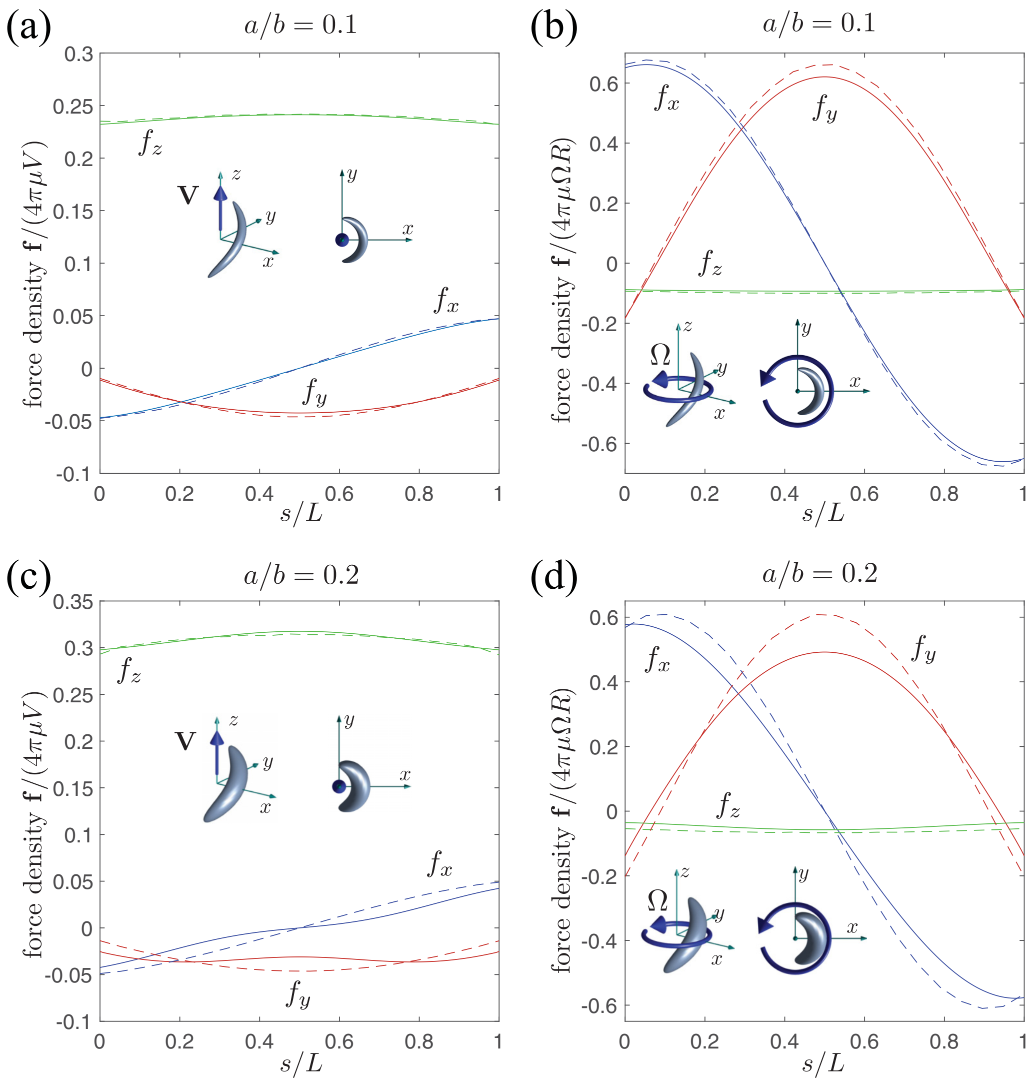

FIG. 2. (a),(b) Distribution of hydrodynamic forces $\mathbf{f}(s)$ along the body centerline of a prolate spheroid (with a slenderness $a/b = 2a/L = 0.1$ and a pitch angle $\theta_0 = \pi/4$) that translates (a) and rotates (b) along its helical axis. The results from the slender body theory (solid lines) and the boundary element method (dashed lines) are both shown as a comparison. The insets show the geometry and motion of the spheroid. (c),(d) The same computation for a thicker spheroid (with a slenderness $a/b = 0.2$).

Here, $\mathbf{R}_\alpha(\mathbf{x}) = \mathbf{x} - \mathbf{x}_0(s_\alpha)$, α denotes the index of the slender body, and $\mathbf{u}_\alpha(\mathbf{x})$ is the ambient flow due to the rest of the slender bodies, which is approximated by their far-field contributions:

$$\mathbf{u}_\alpha(\mathbf{x}) - \mathbf{u}_0(\mathbf{x}) = \frac{1}{8\pi\mu}\sum_{\alpha'\neq\alpha}\int_0^{L_{\alpha'}}\left[\frac{\mathbf{f}(s_{\alpha'})}{|\mathbf{R}_{\alpha'}|} + \frac{\mathbf{R}_{\alpha'}\mathbf{R}_{\alpha'}\cdot\mathbf{f}(s_{\alpha'})}{|\mathbf{R}_{\alpha'}|^3} + \frac{\boldsymbol{\gamma}(s_{\alpha'})\times\mathbf{R}_{\alpha'}}{|\mathbf{R}_{\alpha'}|^3}\right]ds_{\alpha'}. \qquad (11)$$

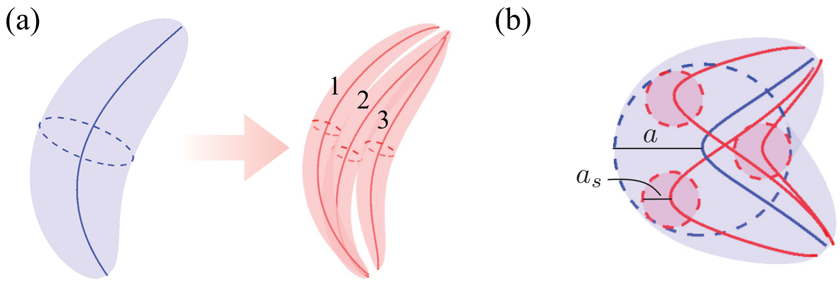

FIG. 3. Schematic drawing of a bSBT representation of an elongated body with a finite aspect ratio. (a) A prolate spheroid (with a slenderness $a/b = 0.25$) is modeled as three fine filaments that can be accessed by the SBT. A view of the middle cross section of this body is shown in (b).

By matching the singular terms with the inner expansion for a single slender body [Eq. (1)], we have the velocity along the αth slender body

$$\mathbf{v}(s_\alpha) - \mathbf{u}_\alpha(s_\alpha) = \frac{1}{8\pi\mu}[\mathbf{A}[\mathbf{f}](s_\alpha) + \mathbf{B}[\boldsymbol{\gamma}](s_\alpha)], \quad \alpha = 1, 2, \ldots, n_s, \tag{12}$$

where $\mathbf{A}[\mathbf{f}](s_\alpha)$ and $\mathbf{B}[\boldsymbol{\gamma}](s_\alpha)$ are respectively the same stokeslet and rotlet terms in the regular SBT [Eq. (4) and (5)]. Given the movement of all bodies $\mathbf{v}(s_\alpha)$, the force distributions (or stokeslets) $\mathbf{f}(s_\alpha)$ are readily solved by the same approach introduced in the regular SBT. In this bundled formulation, the net force and torque become

$$\mathbf{F} = -\sum_{\alpha=1}^{N_s} \int_0^{L_\alpha} \mathbf{f}(s_\alpha) ds_\alpha \tag{13}$$

and

$$\boldsymbol{\Gamma} = -\sum_{\alpha=1}^{N_s} \int_0^{L_\alpha} \big[\mathbf{x}_0(s_\alpha) \times \mathbf{f}(s_\alpha) + g(\phi)\boldsymbol{\gamma}(s_\alpha)\big] ds_\alpha, \tag{14}$$

respectively. It should be noted that the coefficient $g(\phi)$ is present for compensating the reduced cross section area of each filament from the close-packing case. Since the rotlet $\boldsymbol{\gamma}$ is prescribed by the angular velocity and filament radius a_s as $\boldsymbol{\gamma} = 4\pi\mu a_s^2 \boldsymbol{\omega}$, it is maximized at the close-packing case with the fraction factor $\phi = 1$ and $a_s = a_c$, where $a_c = a\,\sin(\pi/N_s)/[1 + \sin(\pi/N_s)]$. To redeem this maximized rotlet without being influenced by the actual dilute packing (constrained by the far-field approximation), we empirically correct the rotlet contribution $\boldsymbol{\gamma}$ as $g(\phi)\boldsymbol{\gamma} = (a_c/a_s)^2\boldsymbol{\gamma}$. This reasoning leads to $g(\phi) = (a_c/a_s)^2 = \left(\frac{1+\phi^{-1}\sin(\pi/N_s)}{1+\sin(\pi/N_s)}\right)^2$ in the above torque formulation.

Accordingly, the flow velocity at any location $\mathbf{u}(\mathbf{x})$ can be expressed as the far-field contribution from all slender bodies:

$$\mathbf{u}(\mathbf{x}) = \mathbf{u}_0(\mathbf{x}) + \frac{1}{8\pi\mu} \sum_{\alpha=1}^{N_s} \int_0^{L_\alpha} \left[\frac{\mathbf{f}(s_\alpha)}{|\mathbf{R}_\alpha|} + \frac{\mathbf{R}_\alpha\mathbf{R}_\alpha \cdot \mathbf{f}(s_\alpha)}{|\mathbf{R}_\alpha|^3} + \frac{\boldsymbol{\gamma}(s_\alpha) \times \mathbf{R}_\alpha}{|\mathbf{R}_\alpha|^3}\right] ds_\alpha. \tag{15}$$

IV. HYDRODYNAMIC DRAGS ON PROLATE SPHEROIDS

We apply both the regular SBT and the bSBT to a prolate spheroid ($a/b < 1$) that translates at a speed V and rotates at a rotation rate ω about its center, which can be exactly solved. We compute its hydrodynamic resistance to translation and rotation in a Stokes flow, and compare them with the analytical solutions [28,29].

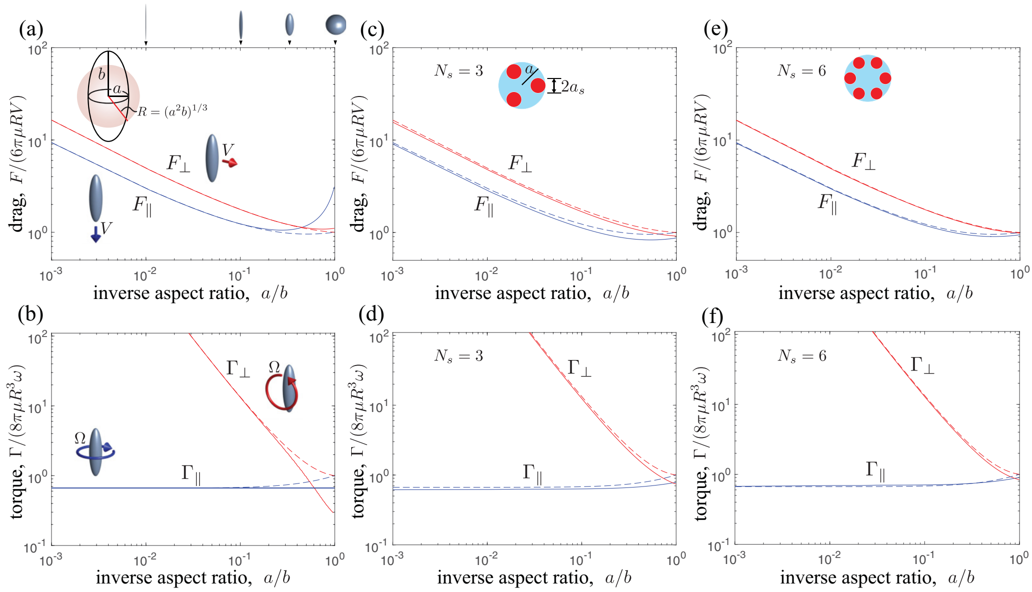

FIG. 4. Translational and rotational drag on a translating and rotating spheroid with its slenderness $a/b < 1$. (a),(b) The force and torque along the longitudinal (blue) and transverse (red) directions, as obtained from the SBT (solid lines). (c),(d) The force and torque along the longitudinal (blue) and transverse (red) directions, as obtained from the bSBT (solid lines) for $N_s = 3$ subunits. (e),(f) The force and torque along the longitudinal (blue) and transverse (red) directions, as obtained from the bSBT (solid lines) for $N_s = 6$ subunits. In (a)–(f), the analytic solutions are shown (in dashed lines) as comparisons.

Figures 4(a) and 4(b) show the computed hydrodynamic force ($\mathbf{F}$) and torque ($\mathbf{\Gamma}$) using the SBT. The dimensionless resistance to translation and rotation are $\mathbf{F}/(6\pi\mu RV)$ and $\mathbf{\Gamma}/(8\pi\mu R^3\omega)$, respectively, where a geometric radius $R = (a^2b)^{1/3}$ is defined uniquely by spheres in equivalent volumes. For a relatively slender spheroid with $a/b \lesssim 0.1$, the SBT results (solid lines) agree extremely well with the analytical solution (dashed lines). When a/b further increases, the SBT results start to deviate from the exact solution, consistent with the above finding for a spheroid with a helical body centerline (Fig. 2). More severely, the longitudinal (blue) and transverse (red) components of the drags are noticeably different when $a/b \approx 1$, disagreeing with the isotropic geometry of the object.

The results from the bSBT are shown in Figs. 4(c)–4(f). For both translation and rotation, the solutions from the bSBT (solid curves) agree reasonably well with the analytical results (dashed line), especially for increasing number of composite filaments N_s. More surprisingly, the difference of the longitudinal and transverse components of such forces or torques is considerably small as a/b approaches unity, agreeing better with the isotropic geometry of a sphere as compared to the SBT result. Despite these agreements with the exact solutions, the drag coefficients from the bSBT are consistently lower, even for $a/b \ll 1$. We expect that this discrepancy is due to far-field treatment of hydrodynamic interactions between the neighboring subfilaments, which is always an approximation due to a finite ratio between the filament radius and their distances.

To further assess the performance of bSBT for an elongated body, we apply both the SBT and the bSBT to objects without axial symmetry. In this case, the drag coefficients become further anisotropic, which can only be characterized by a resistance matrix $\mathcal{M}$, which couples the rotation and translation along all axes. A general form of such a resistance matrix can be shown as

$$\begin{bmatrix}\mathbf{F}\\ \mathbf{\Gamma}\end{bmatrix} = \mathcal{M}\cdot\begin{bmatrix}\mathbf{V}\\ \mathbf{\Omega}\end{bmatrix}, \tag{16}$$

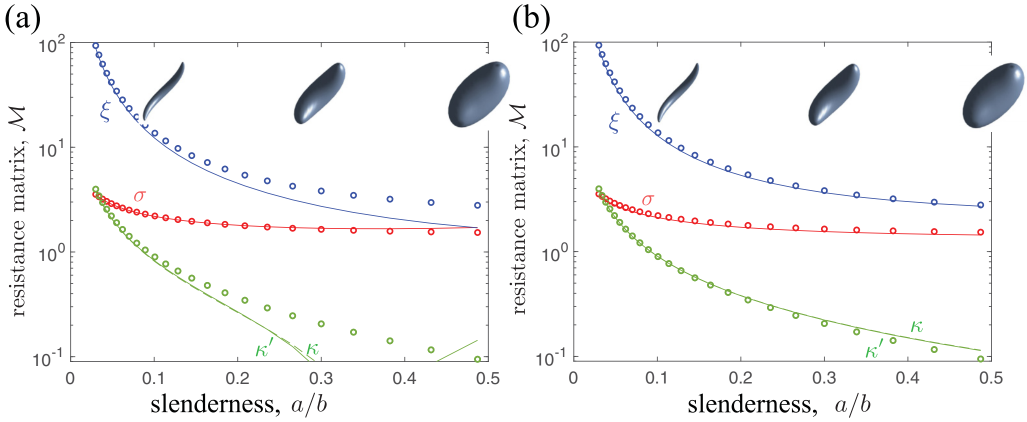

FIG. 5. Resistance matrices of a helical filament at various aspect ratio a/b, as computed by the SBT (a) and the bSBT with $N_s = 6$ subunits (b). The lines in different colors show the ξ (solid blue), σ (solid red), κ (dashed green), and κ' (solid green) elements in the computed matrices [Eq. (17)]. The "exact" solutions as obtained through the BEM are shown in symbols "○" as comparisons.

where $\mathcal{M}$ is a 6×6 symmetric matrix. For benchmarking purposes, we consider again a spheroid with a half-period helical body centerline and a pitch angle $\theta_0 = \pi/4$ (Fig. 2). Here, we let $\hat{\mathbf{z}}$ be the helical axis. For translations at V and rotations at ω about the helical axis, we consider only their coupling with the forces and torques along the same axis. These couplings can thus be described by a 2×2 resistance matrix $\mathcal{M}_z$ as

$$\begin{bmatrix} F_z/(4\pi\mu R) \\ \Gamma_z/(4\pi\mu R^2) \end{bmatrix} = \mathcal{M}_z \cdot \begin{bmatrix} V \\ \Omega R \end{bmatrix} = \begin{bmatrix} \sigma & \kappa \\ \kappa' & \xi \end{bmatrix} \cdot \begin{bmatrix} V \\ \Omega R \end{bmatrix}, \tag{17}$$

where matrix elements σ, ξ, κ, and κ' are dimensionless parameters solely due to geometry.

As shown in Fig. 5(a), we computed the resistance matrix elements $(\sigma, \xi, \kappa, \kappa')$ by the SBT (shown in lines) for a helical filament with its slenderness up to $a/b = 0.5$. Again, the body centerline of the helix is given by $\mathbf{x}_0(s) = 2b\,\sin\theta_0[\frac{1}{\pi}\sin(\frac{\pi s}{L}), -\frac{1}{\pi}\cos(\frac{\pi s}{L}), (\frac{s}{L} - \frac{1}{2})\cot\theta_0]^\top$ with $\theta_0 = \pi/4$. These results were then compared with the fully numerical simulations ("○") through the BEM. Not surprisingly, SBT provides a reasonable estimation when $a/b \lesssim 0.1$. However, for further increased a/b, the predictions from the SBT deviate significantly from the BEM solution, especially for the off-diagonal components (κ and κ'), which start to diverge for $a/b \gtrsim 0.2$.

Similarly, we computed the above resistance matrix through the bSBT for $N_s = 6$ [Fig. 5(b)]. Throughout the entire regime of aspect ratios ($a/b < 0.5$) that we explored, the bSBT (solid and dashed lines) provides reasonable accuracies as compared with the BEM solutions [same as that in Fig. 5(a)]. Moreover, the bSBT retrieves the symmetry of the resistance matrix with the off-diagonal elements κ and κ' consistently equal.

All these results demonstrate that the bSBT can be used to extend the capability of the SBT for a finite elongated object and provide a reasonable accuracy, especially considering their similar order of DOF in computational efforts.

V. ERROR ANALYSIS FOR THE BUNDLED-SLENDER-BODY THEORY

To show how the performance of bSBT varies for various parameters in bundled-slender-body settings, we choose various N_s and ϕ in bSBT and compute the resulting errors by comparing with the full BEM computations. The relative error of bSBT is thus given by $||\Delta\mathcal{M}_z||/||\mathcal{M}_z||$,

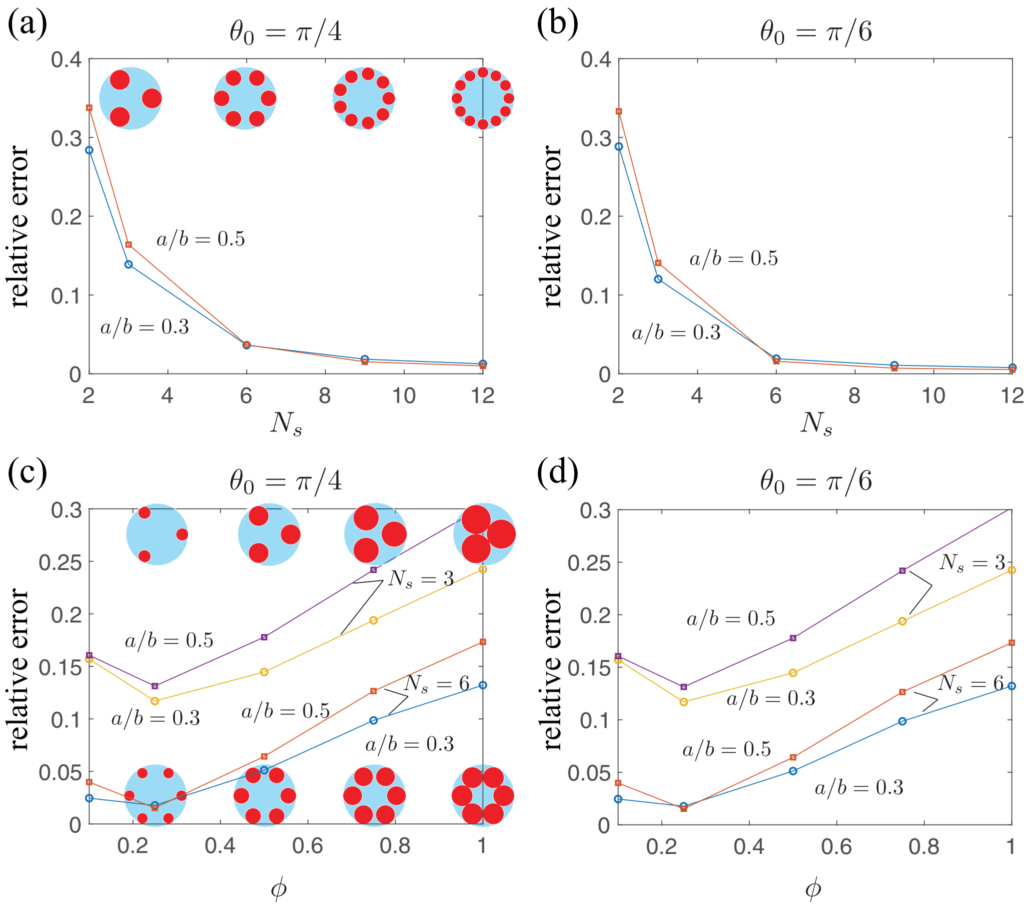

FIG. 6. Relative error in the bSBT results. (a) For a half-period helical spheroid with $\theta_0 = \pi/4$, the relative errors of the bSBT are computed with different number of subunits N_s (insets) for two aspect ratios ($a/b = 0.3$ and $a/b = 0.5$). Here, the fraction factor $\phi = 0.3$. (b) Same computation as (a) for a different helical symmetry ($\theta_0 = \pi/6$). (c) For same geometry as (a), the relative errors by bSBT are shown at various ϕ (insets) in both the $N_s = 3$ and $N_s = 6$ cases. (d) Same computation as (c) for a different helical symmetry ($\theta_0 = \pi/6$).

where $\Delta\mathcal{M}_z$ is the difference between the $\mathcal{M}_z$ calculated in bSBT and BEM, and the symbol $||\cdot||$ corresponds to the norm of the matrix.

Figure 6 shows the relative errors of bSBT for half-period helical spheroids similar to that in Fig. 2, with the body centerlines given by $\mathbf{x}_0(s) = 2b\sin\theta_0[\frac{1}{\pi}\sin(\frac{\pi s}{L}), -\frac{1}{\pi}\cos(\frac{\pi s}{L}), (\frac{s}{L}-\frac{1}{2})\cot\theta_0]^{\top}$. Two different aspect ratios ($a/b = 0.3$ and 0.5) and two different pitch angles ($\theta_0 = \pi/4$ and $\pi/6$) of such geometries are examined accordingly. Not surprisingly, the error of bSBT decreases with increasing N_s [Figs. 6(a) and 6(b)], corresponding to an increase of DOF in the computational space. For varying fraction factors ϕ, the relative error reaches its minimum at $\phi \approx 0.25$ for both $N_s = 3$ and $N_s = 6$, indicating that the subfilaments are sufficiently far apart despite their finite radii [Figs. 6(c) and 6(d)]. The far-field approximation of the neighboring filaments thus still holds in such a dilute configuration. For further decreased area fraction, i.e., $\phi \lesssim 0.25$, the elongated object is expected to be poorly represented by these subfilaments due to the enlarged gaps, leading to an effective “porous” geometry.

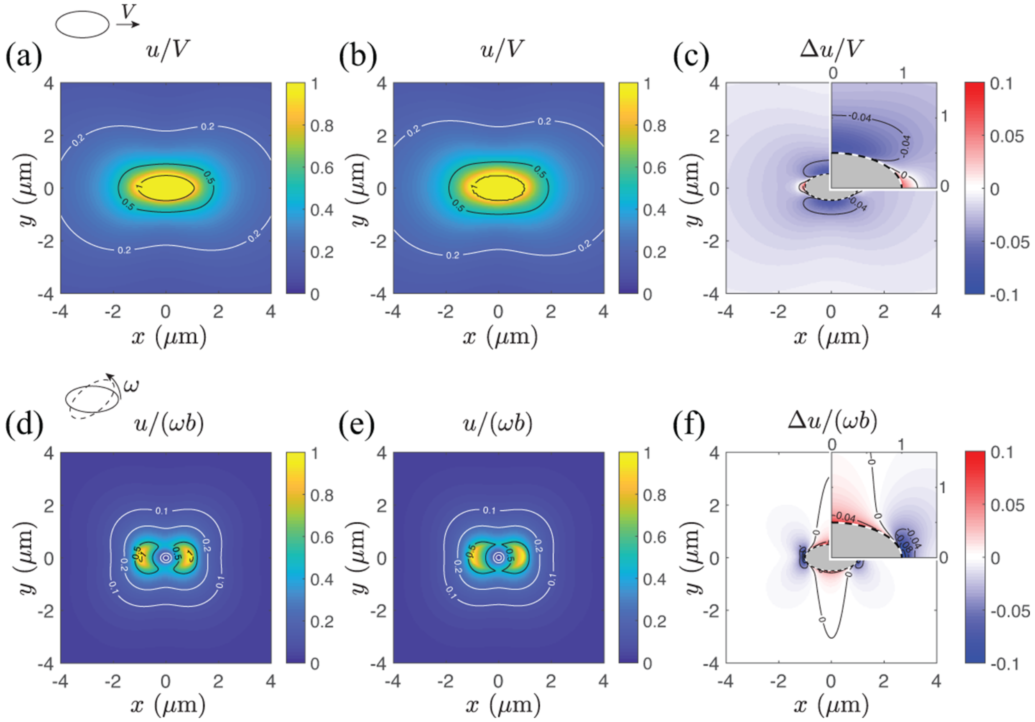

FIG. 7. Comparisons of the flow field of bSBT with the "exact" solutions (obtained by the BEM). (a),(b) The flow field due to a prolate spheroid (with the aspect ratio 2:1 and translating at the speed V) from the bSBT and the exact solution, respectively. (d),(e) The flow field due to the same prolate spheroid rotating at the angular speed ω from the bSBT and the exact solution, respectively. (c),(f) The deviation of the bSBT velocity fields from the exact solutions. The no-slip boundary conditions are roughly satisfied (within a 10% discrepancy) at the spheroidal surfaces.

As shown above, a bSBT setting with $N_s = 6$ and $\phi = 0.25$ provides a decent accuracy without increasing much the DOF in the computational space (due to the moderate N_s), which will be adopted in the rest of this work.

To further illustrate the suitability of the far-field approximation in this bSBT ($N_s = 6$ and $\phi = 0.25$), we compute the flow velocity field due to a moving object, and evaluate its no-slip boundary condition. Here, we consider both the translation (at velocity $\mathbf{V}$) and rotation (at angular velocity $\boldsymbol{\omega}$) of a finite spheroid with $a/b = 0.5$. In both cases, the velocity fields are normalized by the maximum speeds, V and ωb, for translation and rotation, respectively. The flow speed obtained from the bSBT shows a similar profile as that from the BEM (Fig. 7). To estimate the error from the bSBT, we show the flow speed difference between bSBT and BEM [Figs. 7(c) and 7(f)]. Here, the highest discrepancy is within 10% of the maximum speed and the no-slip boundary condition is approximately satisfied at the boundary of the moving object.

VI. HYDRODYNAMICS OF SWIMMING MICROORGANISMS WITH ELONGATED CELL BODIES

Based on the scheme of the bSBT, one can revisit the hydrodynamic problems that can be decomposed into a series of slender bodies. As a useful application, we consider here a swimming bacterium, which is composed of an elongated cell body with a moderate aspect ratio and a fine helical flagellum that approaches an infinite aspect ratio [Fig. 8(a)]. The flagellum is allowed to

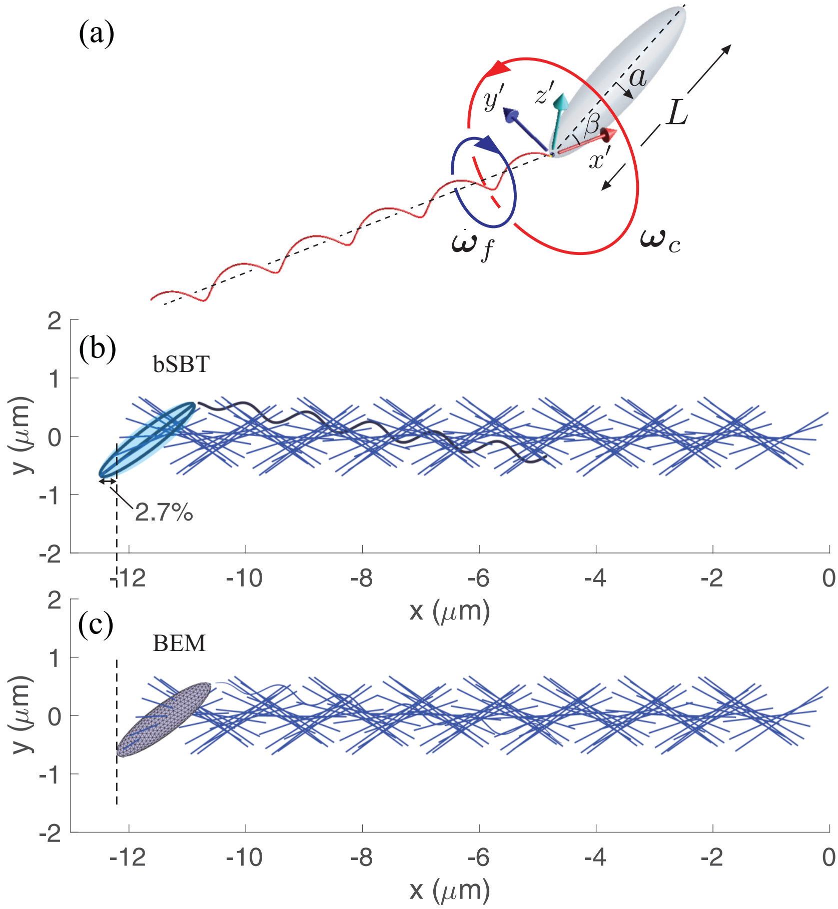

FIG. 8. Hydrodynamic model of a monotrichous bacterium. (a) A schematic diagram of a bacterium with a spheroidal cell body and swimming by rotating a single flagellum. The flagellum is aligned along an arbitrary direction relative to the cell axis, determined by a joint angle β. The relative movement of the flagellum to the counterrotating cell body $\boldsymbol{\omega}_f - \boldsymbol{\omega}_c$ is prescribed by a rotation along the helical axis ($\hat{\mathbf{x}}'$) at the motor speed (ω_0). A 3D trace of the centerline of the cell body with the motor running over 100 revolutions is obtained by the bSBT (b) and the BEM (c). Here, the cell body has a spheroidal shape with its length $L = 2$ μm and radius $a = 0.25$ μm, and the joint angle $\beta = 0.8$ rad. For the BEM, the number of mesh points is set as 2×10^4.

rotate relative to the cell body at a given angular velocity $\boldsymbol{\omega}_0 = \boldsymbol{\omega}_f - \boldsymbol{\omega}_c$, where $\boldsymbol{\omega}_c$ and $\boldsymbol{\omega}_f$ are the angular velocity of the cell body and the flagellum relative to the ambient flow, respectively. The orientation of the cell axis relative to the helical axis of the flagellum ($\hat{\mathbf{x}}'$ in a body-fixed frame of reference) is given by a constant joint angle β, representing the role of a flexible flagellar hook [Fig. 8(a)]. Here, we consider the geometry of a monotrichous bacterium *Caulobacter crescentus*, which swims by rotating a right-handed helical flagellum. The detailed flagellar geometry is given by its length $l_f \approx 6$ μm, thickness $2a_f \approx 20$ nm, helical pitch length $\lambda_f \approx 1.1$ μm, and pitch angle $\theta_f \approx 0.65$ rad [30]. The cell body is modeled as a spheroid with a length $L = 2b = 2$ μm and a slenderness $a/b = 0.25$. The body centerline of the flagellum is prescribed by a helix (along the x' axis) with a vanishing amplitude (characterized by a tapering length $l_d = l_f/2$) toward the cell body:

$$\mathbf{x}'_{f,0}(x') = \lambda_f \left[\frac{x'}{\lambda_f}, \frac{\tanh(x'/l_d)\tan\theta_f}{2\pi} \cos\left(\frac{2\pi x'}{\lambda_f}\right), \frac{\tanh(x'/l_d)\tan\theta_f}{2\pi} \sin\left(\frac{2\pi x'}{\lambda_f}\right)\right]^\top. \tag{18}$$

Given the translational velocity $\mathbf{V}$ at the joint and the angular velocity of the cell body $\boldsymbol{\omega}_c$, the linear velocity along the body centerline of either the flagellum or the cell body becomes

$$\mathbf{v}(s_\alpha) = \mathbf{V} + \begin{cases} (\omega_0 \hat{\mathbf{x}}' + \boldsymbol{\omega}_c) \times \mathbf{x}'_0(s_\alpha), & s_\alpha \in \text{flagellum}, \\ \boldsymbol{\omega}_c \times \mathbf{x}'_0(s_\alpha), & s_\alpha \in \text{cell body}, \end{cases} \tag{19}$$

where α denotes the index of the slender body under the bSBT consideration. These unknown velocities $(\mathbf{V}, \boldsymbol{\omega}_c)$ in the body-fixed frame of reference can thus be readily solved [Eq. (12)], constrained by the force balance and the moment balance requirements as shown in the following:

$$\sum \mathbf{F} = -\sum_\alpha \int_0^{L_\alpha} \mathbf{f}(s_\alpha) ds_\alpha = \mathbf{0}, \tag{20}$$

$$\sum \boldsymbol{\Gamma} = -\sum_\alpha \int_0^{L_\alpha} [\mathbf{x}'_0(s_\alpha) \times \mathbf{f}(s_\alpha) + g(\phi_\alpha)\boldsymbol{\gamma}(s_\alpha)] ds_\alpha = \mathbf{0}, \tag{21}$$

where

$$\phi_\alpha = \begin{cases} 1, & s_\alpha \in \text{flagellum}, \\ 0.25, & s_\alpha \in \text{cell body}. \end{cases} \tag{22}$$

An example of the solutions to the above equations (for joint angle $\beta = 0.8$ rad) is shown in Fig. 8(b). The cell body follows a helical path as shown by the trace of the body centerline [Fig. 8(b)], which agrees decently with the BEM result [Fig. 8(c)]. It can be shown by simple geometric arguments that the pitch of this helical trajectory Λ is determined by the rotation and translation of the cell body as $\Lambda = |\langle \mathbf{V} \cdot \hat{\boldsymbol{\omega}}_c \rangle / (2\pi \langle \omega_c \rangle)|$. The mean displacement of the bacterium over many periods is thus along the axial direction of the helix with its mean velocity

$$\langle \mathbf{V} \rangle = \langle \mathbf{V} \cdot \hat{\boldsymbol{\omega}}_c \rangle \langle \hat{\boldsymbol{\omega}}_c \rangle. \tag{23}$$

In addition to the above swimming kinematics, the bSBT can also be used to resolve the time-dependent structures of the flow surrounding the microorganisms. The flow velocity at any location $\mathbf{x}$ can be obtained through the aforementioned far-field contribution from all slender bodies that compose the bacterium [Eq. (15)]. Figure 9 shows the x-y components of the corresponding flow field, which are made dimensionless by normalizing them with the wave speed of the helical flagellum $\omega_0/k = \omega_0\lambda_f/(2\pi)$. Here, the cell body is aligned along the flagellar axis, i.e., $\beta = 0$. As shown by the instantaneous flow, the bSBT reveals the structured flow field very close to the flagellar filament [Fig. 9(a)]. Despite the parallel alignment of the cell body and its flagellum, the flow field is unsteady, which is expected from the end effect of a finite flagellum filament. A time average of such flow fields also reveals a force-dipole-like structure [Fig. 9(b)], consistent with the earlier experiments [31] and numerical simulations [32].

VII. EFFECT OF CELL GEOMETRIES ON BACTERIAL MOTILITY

In the following, we introduce a curved cell body, reminiscent of the native cell geometry of *C. crescentus* [8]. This cell body is again a prolate spheroid, however, with its body centerline deformed with a uniform radius of curvature r_c. For a finite r_c, the cell-flagellum alignment is determined not only by the joint angle β but also by the circulating direction of the free end of the curved body from the joint. As illustrated in Fig. 10, a circulation following that of the right-handed flagellum leads to a right-handed chirality [Fig. 10(b)], while an opposite circulation leads to a left-handed chirality

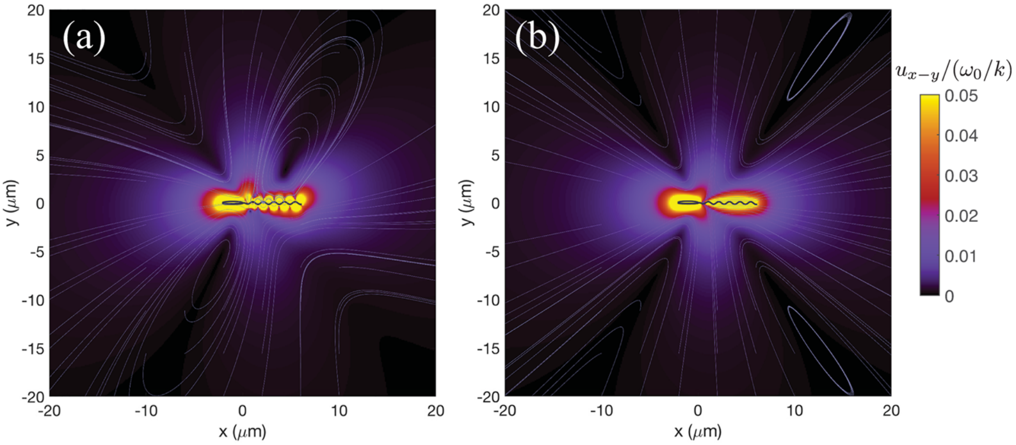

FIG. 9. Computed flow field surrounding a swimming bacterium through the bSBT with $L = 2$ μm, $a = 0.25$ μm, and $\beta = 0$. (a) An example of the instantaneous flow field in the x-y plane exhibits nonaxial symmetry along the swimming direction, corresponding to a time-dependent flow structure. (b) A time-averaged flow from (a) shows an axial-symmetric flow structure associated with a force-dipole moment. Here, the colors show the flow speed $u_{x\text{-}y}$ as normalized by the wave speed ω_0/k of the flagellum. The corresponding streamlines are shown in solid curves.

[Fig. 10(c)]. Their body centerlines (in the body-fixed frame of reference) are thus

$$\mathbf{x}'_{c,\pm}(\varphi) = \mathcal{R}_{y'}(-\beta) \cdot \left[\frac{L}{2} - r_c \sin\varphi, \pm\left(r_c \cos\varphi - \frac{1}{2}\sqrt{4r_c^2 - L^2}\right), 0\right]^\top, \tag{24}$$

where $\varphi \in [-\sin^{-1}\frac{L}{2r_c}, \sin^{-1}\frac{L}{2r_c}]$, $R_{y'}(-\beta)$ represents the rotation about the y' axis by $-\beta$, and the "±" show the chirality ("+": right-handed; "−": left-handed), respectively.

Given these two extreme cases of cell alignments (left-handed vs right-handed), we compute their mean swimming velocities $\langle \mathbf{V} \rangle$ [Eq. (23)] from the bSBT and compare the corresponding speed

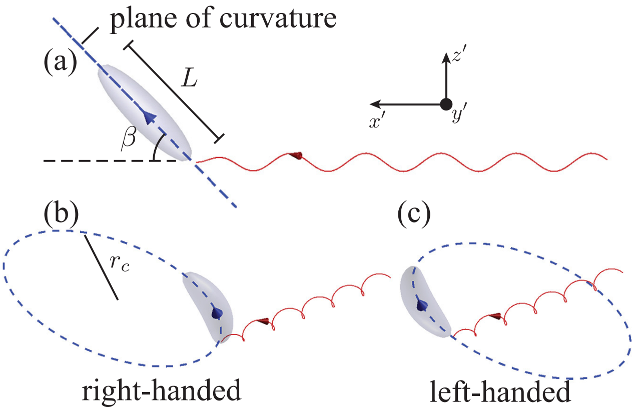

FIG. 10. Curved cell body and its alignment relative to the flagellar axis. While indistinguishable from side views (a), the cell body exhibits either the right-handed (b) or the left-handed (c) chiralities, indicated by a blue arrow moving along its body centerline from the joint to the free end. The dashed circles in blue show the radius of the curvature r_c and the 2D planes where the circular arc lies. Here, the helical flagellum is right handed, indicated by a red arrow oriented along the helix from its back to its front.

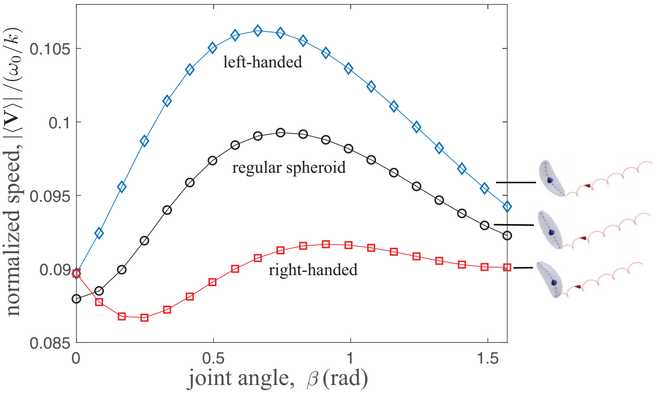

FIG. 11. Motilities of bacteria with curved cell bodies depend on the detailed cell alignments, characterized by the joint angle and the chirality due to the curvature of the body. The left-handed chirality opposite to that of the flagellum, here right handed, leads to higher swimming motilities. A regular spheroid cell body is shown as a comparison.

$|\langle\mathbf{V}\rangle|$ at different joint angle β. Figure 11 shows the result for a curved cell body with $L = 2\ \mu$m, $a = 0.5\ \mu$m, and $r_c = 2\ \mu$m [33]. At $\beta = 0$, the difference due to different chiralities vanishes, and the corresponding swimming motilities are identical. However, as β increases from 0, the motility of the left-handed swimmer is always higher than the right-handed one. In both cases, the motilities reach peaks ($\beta_{\text{peak}} \approx 0.6$ rad and 0.9 rad for the left-handed and right-handed swimmers, respectively), with the left-handed swimmer up to 18% faster than the right-handed one. The distinct motilities for the same cell shape demonstrate the importance of chirality that is embedded in the alignment for a curved cell body.

These motilities for a curved swimmer are also compared with the results from a regular spheroidal cell body ($r_c = \infty$). As shown in Fig. 11, the regular spheroidal swimmer exhibits an intermediate motility as compared with the above two types of curved swimmers, except for small β (i.e., $\beta \lesssim 0.1$ rad). For a vanishing β, the regular spheroidal swimmer swims slowest. This enhanced motility by curvature at $\beta = 0$ is attributed to the increased rotational drag coefficient for a curved cell body. Given a motor speed ω_0, the curved cell body rotates slower (in a direction opposite to that of the motor) than a regular spheroid due to this increase in rotational drag coefficient, leading to a faster flagellar rotation and thus a faster swimming speed in the ambient flow [7,34].

To understand the above distinct effects of cell curvatures on motilities, we examine the swimming kinematics for a curved swimmer in different chiralities. Figure 12 shows the traced body centerlines of the left-handed and right-handed swimmers. For the left-handed swimmer, the tangential directions of the body centerline nearly follow a left-handed helix due to its rotation opposing the clockwise motor. This corkscrewlike configuration leads to a reduction in drag on the cell body. For the right-handed swimmer, this opposite chirality while rotating in the same direction essentially resembles a corkscrew operated in the wrong direction and thus leads to an enhancement in drag on the cell body.

The distinct swimming kinematics are also associated with the different characteristics of the flow fields that surround the swimming bacteria (Fig. 12). On the one hand, the relatively high flow speed is more closely distributed to the proximity of the left-handed swimmer than the right-handed one (in both the longitudinal and transverse directions). On the other hand, the far field with lower flow speed is almost indistinguishable in both cases. This contrast in flow distribution between the near and far field gives rise to an effective localized fluidization for the left-handed swimmer [35], which signifies a higher swimming motility.

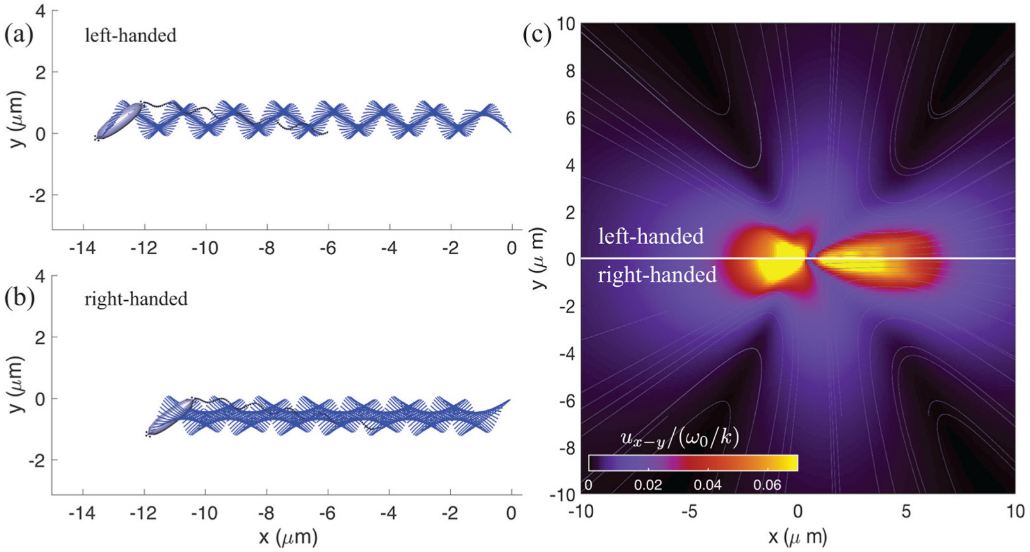

FIG. 12. Cell kinematics and swimming dynamics with identical curvature and joint angle ($\beta = 0.8$ rad) but opposite chiralities in cell alignments. The body centerline of a left-handed cell body composes a double-helix-like envelope (a), while that of the right-handed one composes a complex self-intercepting mesh (b). (c) The time-averaged *x*-*y* flow field surrounding the swimmer with left-handed cell alignment [upper and same as (a)] is more localized than that with the right-handed cell alignment [lower and same as (b)]. Here, the flow speed ($u_{x\text{-}y}$) is normalized by the wave speed of the flagellum (ω_0/k).

VIII. DISCUSSION

We introduce here a methodology in exploiting a SBT for solving Stokes equations for a more general elongated geometry. Here, the elongated geometry is utilized to decompose an object into a bundle of subfilaments along its body centerline. A hydrodynamic problem for this elongated body is thus approximated as a multi-slender-body problem, which is readily solved by the SBT.

Due to the small amount of subfilaments that is typically required for a decent accuracy, the computational DOF for this bSBT essentially has the same order of magnitude as that of the SBT, corresponding to insignificant increases in computational costs. Founded on SBT, this bSBT is fully compatible with any additional slender bodies in a hydrodynamic model, which is ideal for modeling microorganisms with thin motile organelles.

From the applications of this bSBT to a monotrichous bacterium, we show a nontrivial role played by the curvature of the cell body in swimming motility: a finite curvature may enhance or hinder the motility, demarcated by a chirality that emerges from the cell-flagellum coupling. When possessing a handedness opposite to that of the helical flagellum, such a chirality enhances swimming, and vice versa. For a *C. crescentus* bacterium that possesses a flagellum with right handedness, this result suggests a left-handed arrangement in the cell-flagellum alignment for optimized motility. Interestingly, it has been shown that such a left handedness is already embedded in the morphology of *C. crescentus*: its filamented cell body indeed forms a left-handed helix [36]. We suspect that such an intrinsic handedness leads to a left-handed cell-flagellum alignment, which is desired for motility. Nevertheless, our results (Fig. 11) suggest that an optimal joint angle $\beta \approx 0.66$ rad leads to a peak motility for a left-handed *C. crescentus* model. It can be easily shown that this optimal joint angle corresponds to an optimal precession angle of the cell body $\beta' \approx 0.54$ rad, which coincides with the previous experimental measurement on forward-swimming *C. crescentus* ($\beta' = 0.49 \pm 0.15$ rad) [37]. This quantitative agreement suggests that the precession movement of *C. crescentus* is optimized for motility.

So far, the cylindrical-symmetry and far-field approximations in a regular SBT have been inherited directly by the bSBT. These assumptions are potentially violated by the proximity of the neighboring subfilaments, which introduce additional no-slip boundaries. However, we show that an empirically chosen separation among subfilaments (i.e., $0.2 \lesssim \phi \lesssim 0.3$) can provide decent accuracy for the bSBT. This surprising performance potentially results from the fact that the relative velocities among these no-slip boundaries are low due to a rigid-body movement. To further improve the bSBT's performance, these boundary effects need to be thoroughly examined. Moreover, any advances in developing the SBT can be immediately adopted in the bSBT for better outcomes. Analogous to the multibead model [24], including flow asymmetry through higher orders of moment expansions is expected to extend the capacity of the SBT for a single finite filament and a multiple-filament configuration, which both contribute to the development of an advanced bSBT. As an alternative strategy, a no-slip boundary contribution to the bSBT can potentially be formulated as a lubrication-force-type correction [38], which leads to a bSBT in the close-packed configuration (i.e., $\phi \approx 1$). The overall better performance of the bSBT for thinner subfilaments (e.g., Fig. 6) is also consistent with the fact that the orders of accuracy in the moment expansions are mismatched in our SBT formulation: those missing $O(a^2)$ terms are potentially more negligible for relatively thinner subfilaments. In addition, the location of bSBT filaments are not unique by our current definition and can lead to different solutions. Here, we avoid choosing any subtle locations of the filaments (that introduce additional symmetries) only through speculations. For instance, representing a spheroid by a bundle of helical filaments leads to a rotation-translation coupling that is unavailable in the original geometry. A strategy that determines the optimal locations of these filaments is thus needed to minimize any potential errors. We also anticipate that including the aforementioned corrections to slender body approximations and introducing more representative filaments can minimize the difference between different bSBT representations of the same object. All such candidate solutions to improving the bSBT will be explored by our future work.

ACKNOWLEDGMENTS

This work was supported by the National Science Foundation under Grant No. NSF CBET-1706511 and in part by the NSF-CREST: Center for Cellular and Bio-molecular Machines (CCBM) at UC Merced (Grant No. HRD-1547848).

---

[1] E. M. Purcell, Life at low Reynolds number, Am. J. Phys. **45**, 3 (1977).

[2] E. Lauga and T. R. Powers, The hydrodynamics of swimming microorganisms, Rep. Prog. Phys. **72**, 096601 (2009).

[3] H. C. Berg, Bacteria swim by rotating their flagellar filaments, Nature (London) **245**, 380 (1973).

[4] K. D. Young, The selective value of bacterial shape, Microbiol. Mol. Biol. Rev. **70**, 660 (2006).

[5] M. Ramia, Numerical model for the locomotion of spirilla, Biophys. J. **60**, 1057 (1991).

[6] M. Ramia and M. Swan, The swimming of unipolar cells of *Spirillum volutans*: theory and observations, J. Exp. Biol. **187**, 75 (1994).

[7] M. A. Constantino, M. Jabbarzadeh, H. C. Fu, and R. Bansil, Helical and rod-shaped bacteria swim in helical trajectories with little additional propulsion from helical shape, Sci. Adv. **2**, e1601661 (2016).

[8] J. A. Taylor, S. R. Sichel, and N. R. Salama, Bent bacteria: A comparison of cell shape mechanisms in Proteobacteria, Ann. Rev. Microbiol. **73**, 457 (2019).

[9] R. Schuech, T. Hoehfurtner, D. J. Smith, and S. Humphries, Motile curved bacteria are Pareto-optimal, Proc. Natl. Acad. Sci. USA **116**, 14440 (2019).

[10] N. Phan-Thien, T. Tran-Cong, and M. Ramia, A boundary-element analysis of flagellar propulsion, J. Fluid Mech. **184**, 533 (1987).

[11] R. Cortez, L. Fauci, and A. Medovikov, The method of regularized Stokeslets in three dimensions: Analysis, validation, and application to helical swimming, Phys. Fluids **17**, 031504 (2005).

[12] T. Ishikawa, G. Sekiya, Y. Imai, and T. Yamaguchi, Hydrodynamic interactions between two swimming bacteria, Biophys. J. **93**, 2217 (2007).

[13] Y. Hyon, Marcos, T. R. Powers, R. Stocker, and H. C. Fu, The wiggling trajectories of bacteria, J. Fluid Mech. **705**, 58 (2012).

[14] E. E. Keaveny, S. W. Walker, and M. J. Shelley, Optimization of chiral structures for microscale propulsion, Nano Lett. **13**, 531 (2013).

[15] J. Lighthill, Flagellar hydrodynamics, SIAM Rev. **18**, 161 (1976).

[16] J. B. Keller and S. I. Rubinow, Slender-body theory for slow viscous flow, J. Fluid Mech. **75**, 705 (1976).

[17] R. E. Johnson, An improved slender-body theory for Stokes-flow, J. Fluid Mech. **99**, 411 (1980).

[18] S. E. Spagnolie and E. Lauga, Comparative Hydrodynamics of Bacterial Polymorphism, Phys. Rev. Lett. **106**, 058103 (2011).

[19] E. E. Keaveny and M. J. Shelley, Applying a second-kind boundary integral equation for surface tractions in Stokes flow, J. Comput. Phys. **230**, 2141 (2011).

[20] B. Rodenborn, C.-H. Chen, H. L. Swinney, B. Liu, and H. P. Zhang, Propulsion of microorganisms by a helical flagellum, Proc. Natl. Acad. Sci. USA **110**, 1574 (2013).

[21] S. E. Spagnolie, B. Liu, and T. R. Powers, Locomotion of Helical Bodies in Viscoelastic Fluids: Enhanced Swimming at Large Helical Amplitudes, Phys. Rev. Lett. **111**, 068101 (2013).

[22] B. Liu, K. S. Breuer, and T. R. Powers, Helical swimming in Stokes flow using a novel boundary-element method, Phys. Fluids **25**, 061902 (2013).

[23] B. Carrasco and J. García de la Torre, Hydrodynamic properties of rigid particles: Comparison of different modeling and computational procedures, Biophys. J. **75**, 3044 (1999).

[24] M. L. Ekiel-Jeżewska, E. Wajnryb, and F. Feuillebois, Precise multipole method for calculating hydrodynamic interactions between spherical particles in the Stokes flow, Transw. Res. Netw. **37661**, 127 (2009).

[25] D. J. Smith, E. A. Gaffney, J. R. Blacke, and J. C. Kirkman-Brown, Human sperm accumulation near surfaces: A simulation study, J. Fluid Mech. **621**, 289 (2009).

[26] A. Zaritsky, Cell-shape homeostasis in *Escherichia coli* is driven by growth, division, and nucleoid complexity, Biophys. J. **109**, 178 (2015).

[27] C. Pozrikidis, *Boundary Integral and Singularity Methods for Linearized Viscous Flow* (Cambridge University Press, Cambridge, England, 1992).

[28] P. F. Perrin, Mouvement brownien d'un ellipsoide - I. Dispersion diélectrique pour des molécules ellipsoidales, J. Phys. Radium **5**, 497 (1934).

[29] E. W. Small and I. Isenberg, Hydrodynamic properties of a rigid molecule: Rotational and linear diffusion and fluorescence anisotropy, Biopolymers **16**, 1907 (1977).

[30] S. Koyasu and Y. Shirakihara, *Caulobacter crescentus* flagellar filament has a right-handed helical form, J. Mol. Miol. **173**, 125 (1984).

[31] K. Drescher, L. H. Cisneros, S. Ganguly, and R. E. Goldstein, Fluid dynamics and noise in bacterial cell-cell and cell-surface scattering, Proc. Natl. Acad. Sci. USA **108**, 10940 (2011).

[32] J. Hu, M. Yang, G. Gompper, and R. G. Winkler, Modelling the mechanics and hydrodynamics of swimming *E. coli*, Soft Matter **11**, 7867 (2015).

[33] M. T. Cabeen, G. Charbon, W. Vollmer, P. Born, N. Ausmees, D. B. Weibel, and C. Jacobs-Wagner, Bacterial cell curvature through mechanical control of cell growth, EMBO J. **28**, 1208 (2009).

[34] G. Li and J. X. Tang, Low flagellar motor torque and high swimming efficiency of *Caulobacter crescentus* swarmer cells, Biophys. J. **91**, 2726 (2006).

[35] S. A. Mirbagheri and H. C. Fu, *Helicobacter Pylori* Couples Motility and Diffusion to Actively Create a Heterogeneous Complex Medium in Gastric Mucus, Phys. Rev. Lett. **116**, 198101 (2016).

[36] N. Ausmees, J. R. Kuhn, and C. Jacobs-Wagner, The bacterial cytoskeleton: an intermediate filament-like function in cell shape, Cell **55**, 705 (2003).

[37] B. Liu, M. Gulino, M. Morse, J. X. Tang, T. R. Powers, and K. S. Breuer, Helical motion of the cell body enhances *Caulobacter crescentus* motility, Proc. Natl. Acad. Sci. USA **111**, 11252 (2014).

[38] A.-K. Tornberg and M. J. Shelley, Simulating the dynamics and interactions of flexible fibers in Stokes flows, J. Comput. Phys. **196**, 8 (2004).